



Stealth Coronal Mass Ejections from Active Regions

Jennifer O’Kane¹ , Lucie Green¹ , David M. Long¹ , and Hamish Reid² ¹Mullard Space Science Laboratory, UCL, Holmbury St Mary, Dorking, Surrey, RH5 6NT, UK²SUPA School of Physics and Astronomy, University of Glasgow, Glasgow, G12 8QQ, UK

Received 2019 April 11; revised 2019 July 24; accepted 2019 July 24; published 2019 September 5

Abstract

Stealth coronal mass ejections (CMEs) are eruptions from the Sun that have no obvious low coronal signature. These CMEs are characteristically slower events but can still be geoeffective and affect space weather at Earth. Therefore, understanding the science underpinning these eruptions will greatly improve our ability to detect and, eventually, forecast them. We present a study of two stealth CMEs analyzed using advanced image processing techniques that reveal their faint signatures in observations from the extreme-ultraviolet (EUV) imagers on board the *Solar and Heliospheric Observatory*, *Solar Dynamics Observatory*, and *Solar Terrestrial Relations Observatory* spacecraft. The different viewpoints given by these spacecraft provide the opportunity to study each eruption from above and the side contemporaneously. For each event, EUV and magnetogram observations were combined to reveal the coronal structure that erupted. For one event, the observations indicate the presence of a magnetic flux rope before the CME’s fast-rise phase. We found that both events originated in active regions and are likely to be sympathetic CMEs triggered by a nearby eruption. We discuss the physical processes that occurred in the time leading up to the onset of each stealth CME and conclude that these eruptions are part of the low-energy and velocity tail of a distribution of CME events and are not a distinct phenomenon.

Key words: Sun: activity – Sun: corona – Sun: coronal mass ejections (CMEs) – Sun: magnetic fields

1. Introduction

Coronal mass ejections (CMEs) are large eruptions of solar plasma, embedded with the solar magnetic field. Upon occurrence, typically one or more signatures are observed in the lower solar atmosphere, such as filament eruptions, solar flares, post-eruptive arcades, EUV dimmings, and EUV waves that enable the CME source region to be identified (see Webb & Howard 2012, for an overview). Observations from the Earth’s viewpoint mean that a white-light CME with no observable low coronal signatures is normally assumed to be a back-sided event. However, the launch of the twin *Solar Terrestrial Relations Observatory* (*STEREO*) spacecraft (Kaiser et al. 2008) enabled the CME propagation direction to be determined, and therefore the identification of which side of the Sun the CME originated from, using geometric triangulation techniques. Robbrecht et al. (2009) named those eruptions that are seen in coronagraph data but that leave no observable signatures in the low corona as “stealth” CMEs.

Stealth CMEs typically have plane-of-sky speeds less than 500 km s^{-1} (D’Huys et al. 2014) and are frequently found to originate from quiet-Sun regions (Ma et al. 2010) and regions close to open magnetic field (Nitta & Mulligan 2017). They are fairly common; for example, Ma et al. (2010) found that one-third of Earth-sided CMEs at solar minimum had no distinct signatures, while the statistical study of Wang et al. (2011) during the solar minimum of 1997–1998 found that 16% of front-sided CMEs showed no signatures of the eruption on disk. Additionally, Kilpua et al. (2014), in a study of 16 interplanetary CMEs (ICMEs) from 2009, found that 10 ICMEs were stealth events. Despite their slow speeds, stealth CMEs can be the source of geomagnetic activity. Zhang et al. (2007)

studied 77 geomagnetic storms associated with ICMEs that occurred in solar cycle 23. Of these events, nine could not be associated with phenomena occurring on the solar disk. A more recent study by Nitta & Mulligan (2017) focused on a set of stealth events that caused disturbances at 1 au, three of which produced Dst (Disturbance storm time) values greater than -100 nT , indicative of a moderate geomagnetic storm.

The geomagnetic impact and frequency of stealth CMEs have led to growing interest in this type of eruption. There are many open issues, including the fundamental question whether or not stealth CMEs are different from nonstealth events. A review by Howard & Harrison (2013) led the authors to propose that stealth CMEs sit at the lower-energy end of a continuous spectrum of events and originate from streamer blowouts. The authors suggest that the lack of observable signatures is likely due to instrumentation limitations and that the classification of this type of event is a purely observational one. If this is the case, then the trigger and driver mechanisms that are currently proposed for CMEs should be relevant, and once the eruption is underway, observational signatures of the CSHKP standard flare model (Carmichael 1964; Sturrock 1966; Hirayama 1974; Kopp & Pneuman 1976) should be sought with appropriate instrumentation or image processing techniques.

Theories and models of CMEs focus on key aspects such as the specific magnetic configuration of the nonpotential pre-eruptive field (that stores the free magnetic energy used to power the eruption), its evolution due to photospheric flows and/or flux emergence (the energy storage phase), and whether ideal or nonideal processes are able to affect the stability of the field and bring it to the point of eruption (the energy release phase). Models include the breakout model (Antiochos et al. 1999), in which strong shear is invoked within the central arcade of a multipolar system. The shear leads to inflation of the core field followed by reconnection with the overlying arcade. This removes the overlying field and allows the sheared

arcade to erupt if a second phase of reconnection occurs within the sheared arcade, transforming it into a flux rope. The tether cutting model also involves a sheared arcade in which runaway reconnection both builds and ejects the flux rope (Moore et al. 2001). On the other hand, some models require the pre-eruption field to be that of a magnetic flux rope. The flux rope can become unstable owing to the torus instability if the gradient of the field overlying the curved flux rope falls sufficiently rapidly with height (Kliem & Török 2006). Removal of the overlying field, resulting from a nearby CME as in the sympathetic eruption model (Török et al. 2011), may create this condition, as could an increase in flux of the rope, which would raise the structure. A comprehensive review of CME models and their observational indicators may be found in Table 1 in Green et al. (2018).

The challenge then for stealth CME studies is to try to determine whether existing data can be used to investigate the processes involved, and whether aspects of the CME models discussed above are operating. A variety of observational signatures can be utilized to do this. For example, photospheric magnetic field can be used to identify both sustained shear flows along polarity inversion lines and flux emergence. The configuration and evolution of the coronal field can be studied using emission structures observed in EUV or X-ray data. This may include, for example, the identification of a preexisting flux rope in the corona before CME onset through EUV or soft X-ray sigmoidal structures (Green & Kliem 2009; Green et al. 2011; James et al. 2017) and hot flux ropes (Cheng et al. 2011; Zhang et al. 2012; Patsourakos et al. 2013; Nindos et al. 2015). In all these cases, the observed flux rope forms via reconnection either at a low altitude as in the van Ballegoijen & Martens (1989) model or higher up in the corona (James et al. 2017, 2018) with corresponding observational signatures. However, such investigations are predicated on the identification of the correct source region for the stealth CME.

While there are many ways in which a CME can be formed, once the eruption is underway, there is consensus within the community as to how the magnetic field evolves. The erupting structure proceeds through a sequence of distinct evolutionary phases in its kinematics: first, a slow rise of around 10 km s^{-1} , possibly where the stability of the field is lost; second, a rapid acceleration up to velocities of $100\text{--}1000 \text{ s km}^{-1}$ when the main energy release (and magnetic reconnection) occurs; and third, propagation into the heliosphere (Zhang et al. 2001; Zhang & Dere 2006; Vršnak 2008). Any soft X-ray flare emission rises sharply during phase 2, indicating the close coupling between the flare reconnection and CME acceleration. Indeed, phase two can exhibit a variety of observational signatures, which are collectively described by the CSHKP standard model. These signatures include flare reconnection under the erupting structure that produces a post-eruption (flare) arcade and, as the core field expands, the reduction of plasma density in the lower corona (which produces dimming regions). Once the eruption is underway, so by phase 2, all CME models discussed above find that the magnetic configuration is that of a flux rope regardless of the pre-CME field details. Observations of CMEs studied using coronagraph data (Vourlidas et al. 2013) and in situ (Burlaga et al. 1981) indeed find flux ropes in many cases. If stealth CMEs do not differ from other CMEs, it can be expected that they would follow such evolutionary stages, but without obvious flare emission

due to the low-energy release, and exhibit a flux rope configuration as they leave the Sun.

There is yet to be a clear definition of stealth CMEs, with some works stating that a stealth CME is one with no low coronal signatures, while other works define a stealth CME as one with no obvious, or very weak, low coronal signatures. Although the differences between these two classifications may at first seem trivial, stating that there are no signatures at all suggests that the signatures simply do not exist. On the other hand, if they are events with very weak and/or no obvious signatures, the events may not necessarily be fundamentally different from other CMEs, and work toward producing tools and techniques that reveal these weaker signatures can progress. A comprehensive study by Alzate & Morgan (2017) showed, using advanced imaging processing techniques applied to coronal observations, that all 40 stealth CMEs in a catalog developed by D’Huys et al. (2014) did indeed manifest themselves with one or more lower coronal signatures. This suggests that the source regions of stealth CMEs can be found and studied.

The aim of this study is to combine knowledge of the observational signatures of CMEs related to the formation and eruption of nonpotential fields with the latest image processing techniques to extend the study of Alzate & Morgan (2017) for two stealth CME events. Stealth event 1 occurred on 2009 October 27, and stealth event 2 occurred on 2011 March 3. Both events have had their approximate source region determined using triangulation by Kilpua et al. (2014) and Pevtsov et al. (2012), respectively. We aim to investigate whether these stealth CMEs show signatures of the CSHKP standard model, albeit faint, in order to identify the exact source region. We then look for signatures of the processes that could account for the formation and destabilization of the eruptive structures. In Section 2 we describe data used and our analysis techniques. Section 3 displays our findings for the two stealth CME events, and these are discussed in Section 4. Conclusions are presented in Section 5.

2. Observations and Methods

This work uses data from the Atmospheric Imaging Assembly (AIA; Lemen et al. 2012) on board the *Solar Dynamics Observatory* (SDO; Pesnell et al. 2011), the Extreme Ultraviolet Imager (EUVI; Howard et al. 2008) on board *STEREO* (Kaiser et al. 2008), and the Extreme ultraviolet Imaging Telescope (EIT; Delaboudiniere et al. 1995) on board the *Solar and Heliospheric Observatory* (SOHO; Domingo et al. 1995). Photospheric line-of-sight magnetograms are obtained from the Helioseismic and Magnetic Imager (HMI; Scherrer et al. 2012) and the Michelson Doppler Imager (MDI; Scherrer et al. 1995) on board *SDO* and *SOHO*, respectively. The CMEs are identified using data from the white-light coronagraphs, the Large Angle and Spectrometric Coronagraph (LASCO; Brueckner et al. 1995) and COR1/COR2 (part of the SECCHI instrument suite; Howard et al. 2008) on board *SOHO* and *STEREO*, respectively. The details of instruments used in each stealth CME event are outlined in Table 1.

The graduated cylindrical shell (GCS) model and stack plots of EUVI and COR1 were used to trace the CME back to the start of the eruption. In order to increase the likelihood of being able to identify lower coronal signatures of the stealth CMEs in EUV data, the Multi-scale Gaussian Normalization technique

Table 1
Details of the Instruments Used within This Study

Instrument/Spacecraft	Type	Used for Event	Wavelengths (Å)	Resolution (arcsec)	FOV (R_{\odot})
EIT/ <i>SOHO</i>	EUV imager	SE1	195	5.2	0–1.5
MDI/ <i>SOHO</i>	Magnetogram	SE1	N/A	4	0–1
LASCO C2/ <i>SOHO</i>	WL coronagraph	SE2	N/A	47	1.5–6
EUVI/ <i>STEREO</i>	EUV imager	SE1, SE2	195, 304	3.2	0–1.7
COR1/ <i>STEREO</i>	WL coronagraph	SE1, SE2	N/A	15	1.5–4
AIA/ <i>SDO</i>	EUV imager	SE2	94, 131, 171, 193, 211, 304	1.2	0–1.5
HMI/ <i>SDO</i>	Magnetogram	SE2	N/A	1	0–1
Nançay Radioheliograph	Radio Interferometer	SE2	150 MHz	200	0–2

Note. SE1 = stealth event 1, 2009 October 27. SE2 = stealth event 2, 2011 March 3.

(MGN; Morgan & Druckmüller 2014) was applied and running difference images were created for both events and examined for dimming regions. The radio data were imaged using the Nançay Radioheliograph (NRH; Kerdraon & Delouis 1997).

2.1. GCS Model

The GCS model is an empirical model developed by Thernisien et al. (2006). It is used to study the 3D morphology, position, and kinematics of flux rope CMEs. Flux rope CMEs typically have a three-part structure: a bright leading front, a dark cavity, and a bright core, where the dark cavity is representative of a flux rope within the CME structure. The geometry of the model includes cone-shaped legs, a pseudo-circular front, and a circular cross section, fitted by eye using at least two different vantage points and six parameters: longitude, latitude, height, tilt angle, half angle, and ratio. The resulting GCS model is a shape similar to that of a hollow croissant, which expands in a self-similar way. The model requires at least two coronagraph images from two different spacecraft (e.g., COR2-A and COR2-B) taken at the same time.

The GCS model used COR1 and COR2 data to find the approximate source region for each stealth CME. A radial path away from the Sun is assumed; however, it is noted that many CMEs in these lower regions are nonradial with respect to their source regions (Cremades & Bothmer 2004; Cremades et al. 2006).

Typically when fitting the GCS model to the coronagraph images, one would also ensure that the flux rope footpoints from the model match up with those determined observationally in the EUV images. Due to stealth CMEs having no obvious low coronal signatures, it is an opportunity to obtain an approximation of the location of the CME footpoints and thus the source region of the CME. However, due to both limitations with the model and possible alterations in CME direction after eruption, the source region obtained from the GCS model may not be exactly correct. Therefore, it is necessary to also search for observational signatures of the eruption.

2.2. Observations

Stack plots of COR1 and EUVI were created for both events. The slices generated from the stack plots were radially outward from the Sun. In each case, stack plots were created for all angles that crossed the CME structure at a variety of angular widths, as observed in COR1 field of views. All stack plots were examined for potential activity. The stack plots presented in this paper are

the radial slices that intersect through the center of the concave-up structure, assumed to be the flux rope cavity, as this showed the most clear propagating CME structure.

For each instrument, a variety of difference imaging techniques were employed at various temporal separations. The running difference and running ratio images gave the best result for our work. The running difference subtracts a following image from a leading image, while the running ratio divides a leading image from a following image. Temporal separations varied between 2 minutes and 3 hr. Thirty minutes proved to provide a clearer image, for capturing the dynamic motions, without having too much effect on the ambient background, while 3 hr proved best for capturing faint EUV dimmings. The first event studied here occurred on 2009 October 27 and was observed by *SOHO* and both *STEREO* spacecraft. The separation angle between *STEREO-A* and *STEREO-B* was 123° , with *STEREO-B* 60° behind Earth and *STEREO-A* 63° ahead of Earth (left panel of Figure 1). For this event, one of the EIT wave bands was used and two of the EUVI wave bands were used (see Table 1). For EIT we used 12-, 10-, and 30-minute temporal separations. The second event studied here occurred on 2011 March 3 and was observed on disk by *SDO* and at the limb by both *STEREO* spacecraft. At this time the separation angle between *STEREO-A* and *STEREO-B* was 178° , with *STEREO-B* 95° behind Earth and *STEREO-A* 87° ahead of Earth (right panel of Figure 1). Running time difference images were created for six of the AIA wave bands and for two of the EUVI wave bands, as outlined in Table 1. For each of the AIA passbands we used 2-, 5-, and 10-minute temporal separations. For each of the EUVI passbands we used 5-, 10-, and 30-minute temporal separations. Longer temporal separations were necessary in order to observe dynamic structure of the stealth CMEs, which evolve at a relatively slow rate. Temporal separations were chosen based on the cadence of each instrument. The temporal evolution of the CME as it propagates outward from the Sun was tracked using a stack plot that combined the fields of view of both EUVI and COR1 from the *STEREO* spacecraft.

The MGN technique was applied to each of the EUV passbands listed in Table 1. This technique reveals faint structure in the low corona that is usually hidden as a result of bright regions that dominate over regions of the Sun with lower EUV emission. The ability to observe this fine structure is obtained by normalizing images at multiple spatial scales, using the local mean and standard deviation, and producing a weighted combination of the normalized components. The

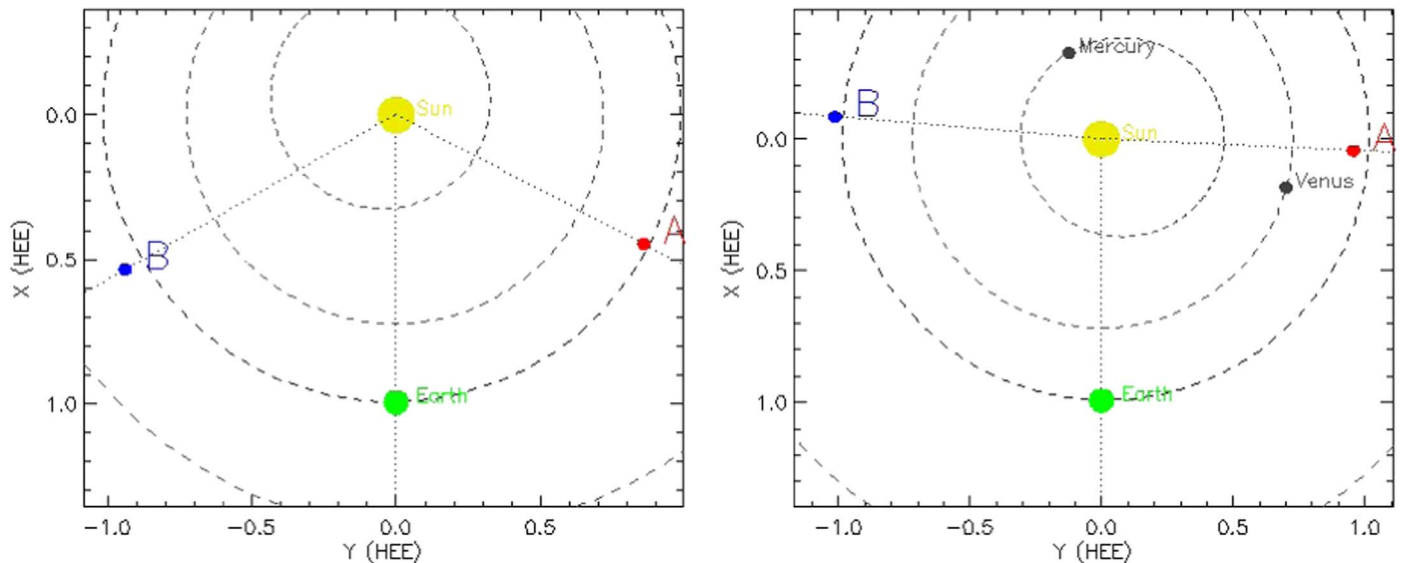


Figure 1. Positions of *STEREO-A* and *STEREO-B* on 2009 October 27 (left) and 2011 March 3 (right).

method produces detailed images similar to wavelet-based techniques (Stenborg & Cobelli 2003; Stenborg et al. 2008) and the noise adaptive fuzzy equalization technique (Druckmüller 2013); however, MGN is much more computationally efficient, faster by at least an order of magnitude, and does not require a high-performance computer. The detailed images produced by this technique can reveal fine structural changes in the low corona that are related to the formation and later eruption of the stealth CME.

Running ratio images with 3 hr temporal separations were used, in order to identify, track, and enhance any EUV dimmings associated with the stealth CMEs. Edges of dimmings were manually selected every half hour, and the contours of the dimming regions at each time are plotted.

MDI and HMI were used to observe the evolution of the photospheric magnetic field for the 2009 October 27 and 2011 March 3 stealth CMEs, respectively. We searched for changes in the magnetic field such as flux emergence, flux cancellation, and shearing motions that may play an important role in the formation and initiation of CMEs, as well as observing the configuration of the magnetic field at the time of eruption.

The NRH was used to analyze the radio emission that arose during the 2011 March 3 stealth event. The radio images were made using the NRH clean algorithm from data with a 1 s cadence. The radio flux was calculated from the images using a box of length $600''$.

3. Results

3.1. Stealth Event 1: 2009 October 27

On 2009 October 27 the *STEREO* coronagraphs observed a CME that was found by Kilpua et al. (2014) to be Earth directed, but without any low coronal signatures. The authors reported that the CME first appeared in *STEREO-B* (*STEREO-A*) COR1 at 10:30 UT (15:30 UT) on 2009 October 27, giving an estimated eruption onset time of $\sim 06:00$ UT 2009 October 27. The CME had a plane-of-sky speed of 208 km s^{-1} as seen by *STEREO-A*.³ Kilpua et al. (2014) performed a multispacecraft forward-modeling analysis using the GCS model and

applied a triangulation technique, approximating the source region of the event to be located at N03W06 and N03W10, respectively, from the two methods. Although eruptive signatures were observed on the solar disk, the authors concluded that this activity was not cospatial with the approximated source region of the stealth CME. Instead, the estimated source region is approximately halfway between two active regions (ARs), one in its emergence phase (AR 11029) and one in its decay phase with no NOAA AR number assigned.

3.1.1. Analysis

Stack plots were created to track the CME through the coronagraph and EUV data, to the surface of the Sun. Figure 2 shows the stack plot created using a slice of the data at an angle of 80° from solar north in the clockwise direction. The propagation of the concave-up section of the CME is clearly visible in the COR1-A stack plot created from a time series of these data slices, where the CME appears to exhibit a slow-rise phase that is in progress by 23:00 UT 2009 October 26, followed by a phase of rapid acceleration at $\sim 13:00$ UT 2009 October 27. However, the EUVI-A stack plot does not show any clear upward-propagating structure. The result that it was unable to be picked up in the field of view captured by EUVI-A, combined with the observation of the slow-rise phase in the COR1 field of view, suggests that the eruption was initiated from higher altitudes. The EUVI stack plot does, however, show a large brightening around the time of the rapid acceleration phase beginning, likely to be post-eruption loops associated with the stealth CME. We then fitted exponential and quadratic curves to the CME position in the COR1 field of view. The curves can give indications of what mechanisms are driving the eruption (Schrijver et al. 2008; D’Huys et al. 2014). Numerical simulations matched with observations have demonstrated that an exponential rise profile occurs when an instability is dominating the eruption, such as the torus or kink instability, while a quadratic rise profile occurs during a breakout model scenario. For this event the exponential curve produced the best fit, suggesting an instability dominating the eruption. Both the torus and kink instability require a flux rope

³ <http://solar.jhuapl.edu/Data-Products/COR-CME-Catalog.php>

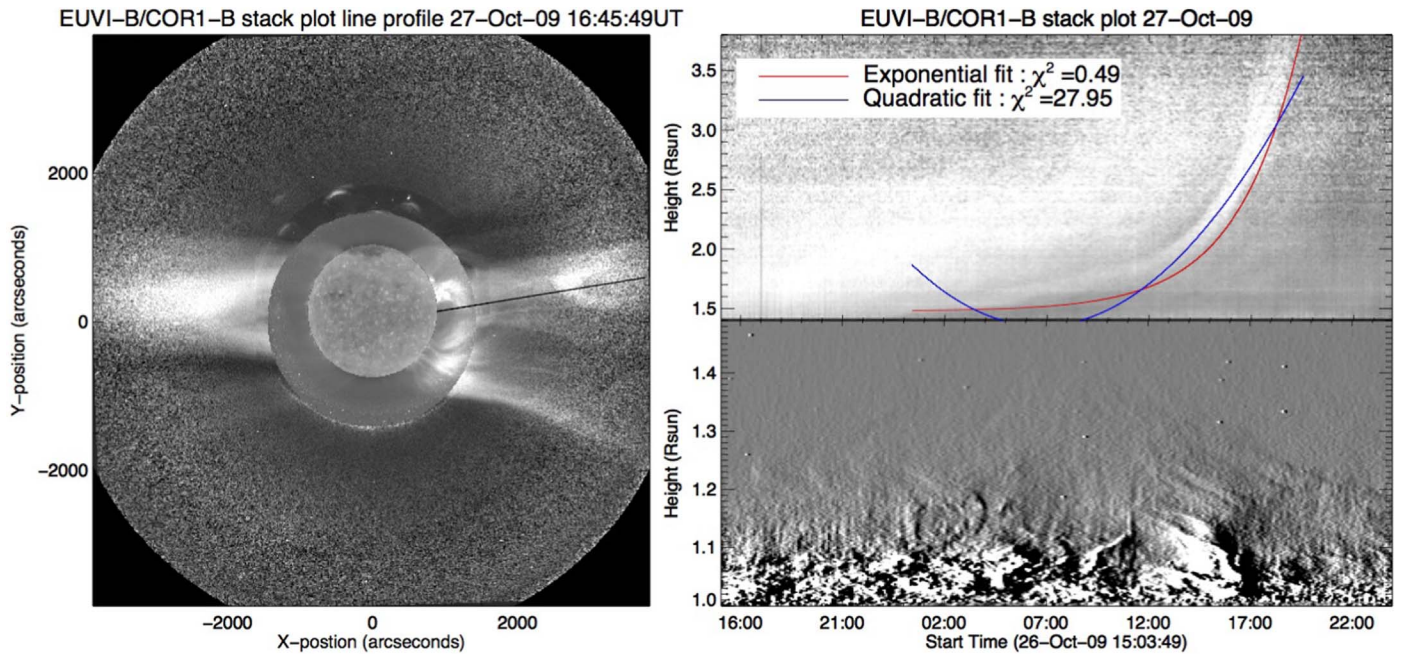


Figure 2. Left: EUVI/COR1 image indicating the slice used to create the stack plot (solid line). Right: EUVI-B 195 Å (lower) and COR1-B (upper) stack plots. The height–time profile of the stealth CME observed on 2009 October 27 can be determined from the COR1-B data, which show the underside (concave-up structure) of the stealth CME. Exponential (red line) and quadratic (blue line) fits have been applied to the COR1-B data.

prior to eruption, and given that the concave-up structure could be tracked for a period of hours during the slow-rise phase, it is likely that in addition to the structure being initiated at a high altitude, the flux rope was also formed at a high altitude in the corona.

The stealth CME is not observed in the COR1-A images until $\sim 15:30$ UT on 2009 October 27, several hours after the eruption onset time as determined by Kilpua et al. (2014). The CME is also very faint and barely visible in the images, making it difficult to pinpoint the exact time that it enters the field of view. It also emerges from a bright streamer that acts to mask the CME structure. However, the stealth CME is seen more clearly, and earlier, in COR1-B, which could suggest that the eruption is closer to the limb of *STEREO-B* than *STEREO-A*. The estimated source region from triangulation techniques is of similar distance to the nearest limbs in both spacecraft, while the decayed AR is directly on the limb in *STEREO-A* and on disk in *STEREO-B*, and AR 11029 is directly on the limb of *STEREO-B* and on disk in *STEREO-A*.

Using COR1 and COR2 from the twin *STEREO* spacecraft, the wire frame of the GCS model (representing the flux rope) was fitted to the concave-up cavity structure in the coronagraph observations (Figure 3). The footpoints of the erupting structure were found to be N03E05 and N03W18 from the GCS model, illustrated by the blue crosses in Figure 4, centered around the region approximated by Kilpua et al. (2014) (red cross in Figure 4) using the triangulation and the GCS model. This approximated source region is located in a quiet-Sun region in the northern hemisphere. On the east and west sides of the approximated source region were a decayed AR and NOAA AR 11029, respectively (Figure 4).

We then applied the MGN technique to the EUV data and additionally produced running difference images using the EUV data, enabling a variety of dynamical structures to be observed in the lead-up to and following the stealth CME. The

activity in the decayed AR can be summarized as follows: a large and clear eruption beginning at $\sim 11:25$ UT 2009 October 26 as seen in *STEREO-A* EUVI data with an associated white-light CME observed in COR1-A at $\sim 12:00$ UT (Figure 3, first panel); a very faint structure that moves outward through the field of view of *STEREO-A* COR1 at $\sim 21:00$ UT 2009 October 26, which may be a part of the previous event or a separate eruption that closely follows the former; an extremely faint rising loop at $\sim 07:10$ UT that cannot be followed to the edge of the field of view of EUVI—since no associated post-eruption loops were observed, it is deemed to be a failed eruption. None of these activity events can be shown to be associated with the stealth CME, and therefore the decayed AR is not deemed to be its source region. The activity in AR 11029 in the ~ 1.5 days before the stealth CME was first observed in coronagraph data and can be summarized as follows: small burst of bright plasma in the north of the AR at $\sim 21:45$ UT 2009 October 26; expanding loops begin forming early on 2009 October 27 to $\sim 05:10$ UT; and multiple C-class flares between 18:38 UT on 2009 October 26 and 11:07 UT on 2009 October 27 (Figure 3, second panel). During this time, AR 11029 continues to brighten and displays an ongoing reconfiguration of the loops, which may be associated with the ongoing flux emergence in the region. There is a weak dimming region to the north of the AR and on its western side seen in EIT data that begins at $\sim 06:30$ UT 2009 October 27; however, neither running difference nor running ratio images could enhance this to a trackable feature. By $\sim 12:55$ UT AR 11029 continues to brighten, with new loops forming. From the location of AR 11029, along with the observed dimming and reconfigured field, we conclude that this is the most likely source region of the stealth CME on 2009 October 27.

Finally, we looked into the evolution of the photosphere. The red cross in Figure 4 indicates the source of the stealth CME as estimated by Kilpua et al. (2014), while the blue crosses

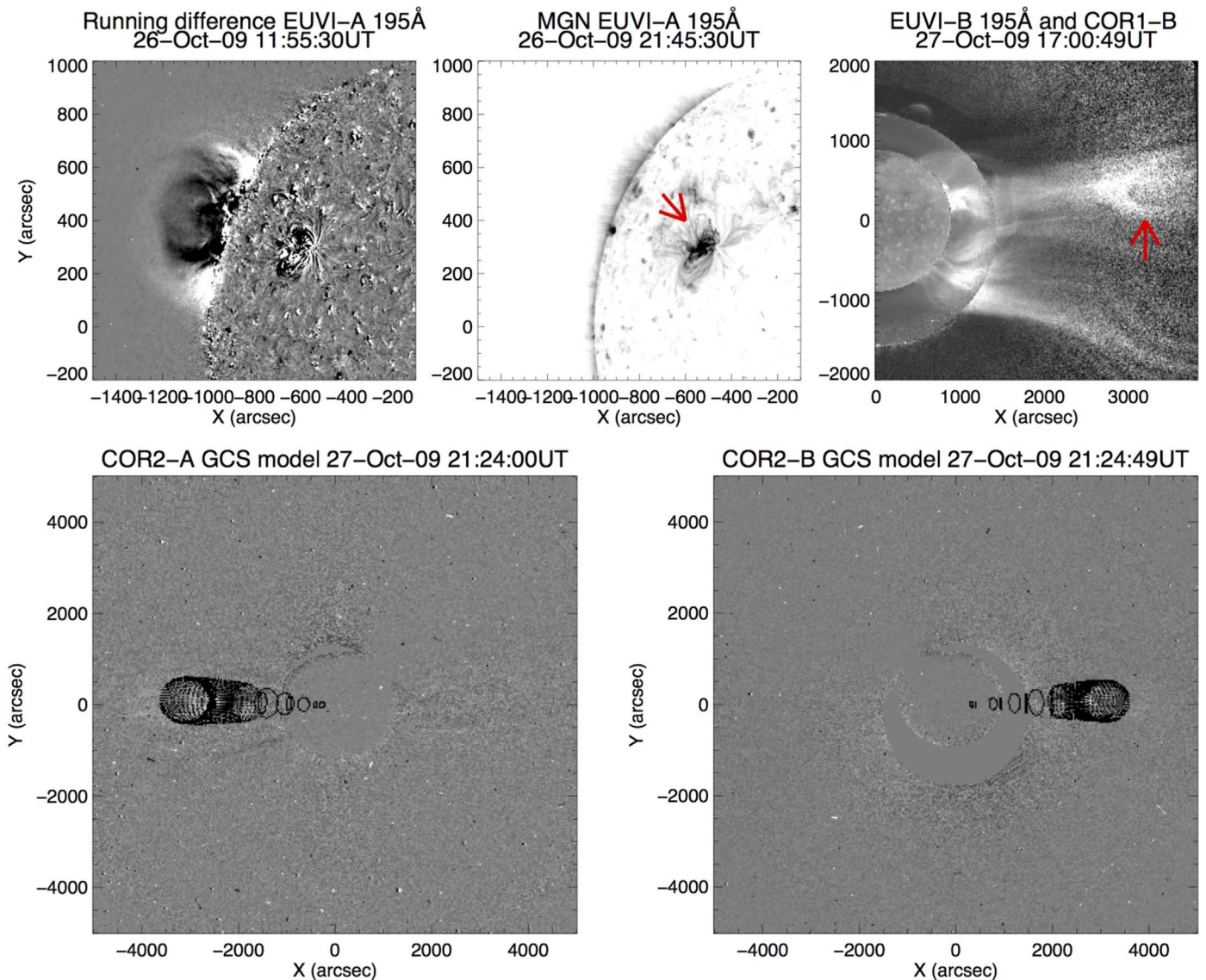


Figure 3. Top left: EUVI-A 195 Å running difference image with a 5-minute temporal separation, showing an eruption from the decayed AR. The eruption occurs several hours before the eruption of the stealth CME. Top middle: MGN-processed EUVI-A 195 Å showing a small eruptive burst of plasma from the newly emerged AR, believed to be the source of the stealth CME. Top right: combined EUVI-B 195 Å and COR1-B image. The CME is indicated by the arrow and has a dark cavity, indicative of a flux rope present in the CME. Bottom: wire frame fitted to the CME in COR2-A (left) and COR2-B (right).

indicate the approximate footpoints of the CME found from the GCS model. The approximated source location is an area of weak dispersed field with no clear polarity inversion line, reinforcing the conclusion that the stealth CME originated from a nearby AR. AR 11029 first starts to emerge early on 2009 October 22 in the eastern hemisphere, into a region of weak mixed polarity field. The AR builds up as a result of the emergence of several bipoles that coalesce. A second bipole begins to emerge at $\sim 03:00$ UT 2009 October 24 on the northwestern side of the first bipole. A third bipole begins its emergence at $\sim 10:00$ UT 2009 October 26 at the polarity inversion line of the second bipole. Flux emergence is still underway at the time of the stealth CME as determined using the EUV data. At the time of the eruption the AR has a beta-gamma configuration according to the Hale classification scheme (Hale et al. 1919), meaning that the region was bipolar

overall but no continuous line could be drawn separating spots of opposite polarities.

3.1.2. Overall Remarks

The combined analysis of the photospheric magnetic field, activity in the lower corona, and CME propagation as seen in coronagraph data together suggest that the stealth CME of 2009 October 27 originated in AR 11029. The CME is observed to be in its slow-rise phase as observed by *STEREO-B* COR1 data by 23:00 UT 2009 October 26. The fast-rise phase is observed to start around 13:00 UT 2009 October 27, similar in time to the formation of new loops in the AR, which are deemed to be post-eruption loops. The time of the fast-rise phase onset is ~ 7 hr later than the estimated time of eruption determined by Kilpua et al. (2014). This discrepancy may be partly due to the stealth CME originating from a high altitude, as determined from the

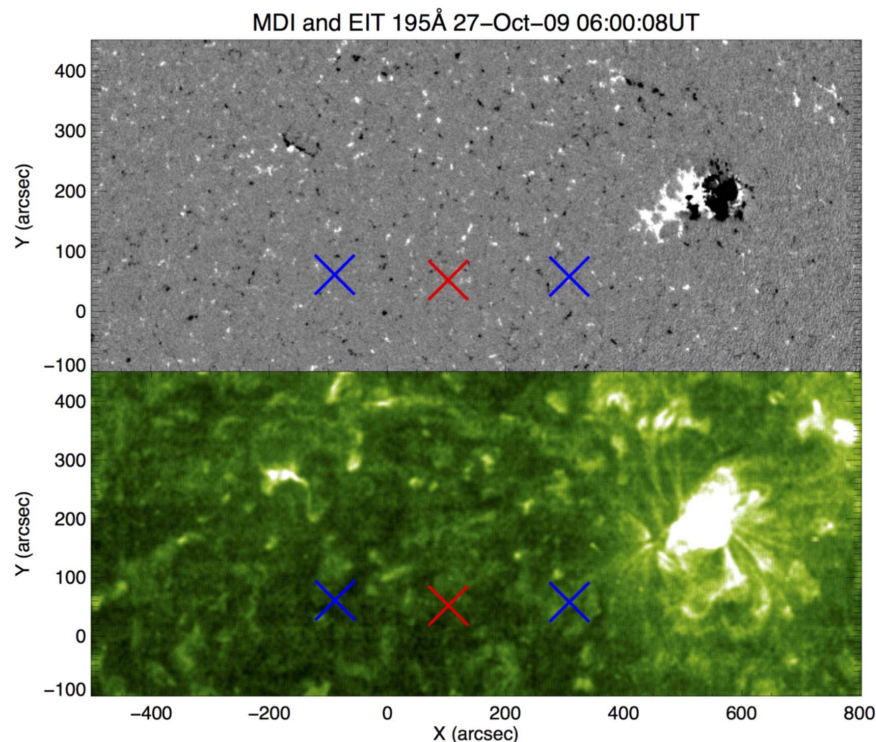


Figure 4. Top panel: MDI magnetograph image. Bottom panel: MGN-processed EIT 195 Å image. The triangulated source region determined by Kilpua et al. (2014) is illustrated by the red cross. The footpoints of the eruption approximated by the GCS model are illustrated by the blue crosses. The estimated source region is located in a region of highly dispersed magnetic field, with no polarity inversion line, suggesting that an eruption is unlikely to have occurred here. A small decayed AR is located northeast and a newly emerged AR (NOAA AR 11029) is located northwest of the estimated source region.

absence of any signature of the erupting CME in EUV data, and only the underside of the CME being observable in COR1 data.

3.2. Stealth Event 2: 2011 March 3

On 2011 March 3 the *STEREO* coronagraphs observed an Earth-directed CME with a faint leading edge that appeared to be slowly rising in *STEREO-A* COR1 data from around 00:00 UT. Despite the faint leading edge, the CME is seen to have a clear circular shape, the concave-up section of which was first observed in *STEREO-A* COR1 at approximately 03:00 UT on 2011 March 3. The CME had a plane-of-sky speed of 409 km s^{-1} as seen by *STEREO-A*.⁴ The LASCO coronagraphs observed this CME as a faint partial halo that propagated to the south. This stealth CME was previously studied by Pevtsov et al. (2012), who found, using a triangulation approach, the CME source region to be S35W10. In the vicinity of the approximated source region was a small AR (NOAA AR 11165) and a filament channel as can be seen in Figure 5. Pevtsov et al. (2012) concluded that the filament channel was the CME source region. Nitta & Mulligan (2017) find two EUV dimmings centered around S20, the region in which the AR was present. The source region was on disk from the *SDO* perspective and at the solar limb from the perspective of both *STEREO* spacecraft. This means that the combined AIA and EUVI data allow the approximated source region to be studied when viewed at the limb, as well as from above. However, as detailed below, the *STEREO-A* EUVI data show more clearly the evolution and eruption of the source region and are focused on in this study.

3.2.1. Analysis

The stack plot shown in Figure 6 used a slice of the EUVI data and COR1 located at an angle of 240° clockwise from solar north (indicated by the black line in the left panel). The propagation of the concave-up section of the CME is clearly visible in the COR1-A stack plot (top panel of Figure 6) but shows that the slow-rise-to-fast-rise transition was not captured. The slow-rise-to-fast-rise transition of the underside of the CME was not visible in the EUVI data, presumably because of insufficient plasma emission. This, combined with little to no structure observed in the EUVI, may be the result of the CME being initiated from a high-altitude structure with weak plasma emission. Although the CME propagation profile was fitted with an exponential and a quadratic curve, neither curve fits the CME curve better than the other, and therefore no conclusions on the most likely initiation mechanism can be made from this.

The GCS model was applied in the same way as discussed previously (Figure 7). The footpoints of the eruption from the GCS model were found to be S18E04 and S16W18, illustrated by the blue crosses in Figure 5. This was to the east and west of the small AR (NOAA AR 11165), and further north than the region triangulated by Pevtsov et al. (2012). The footpoints are of a similar location to the dimmings found by Nitta & Mulligan (2017) centered around S20.

The MGN-processed AIA 211 Å images show dynamic plasma emission structures that occur around AR 11165. Likewise, MGN-processed images and running difference images with a 30-minute temporal separation from EUVI-A 195 Å show a number of dynamic structures located off-limb and out to the edge of the field of view above AR 11165. Comparing 195 Å EUVI-A and AIA 211 Å observations, we

⁴ <http://solar.jhuapl.edu/Data-Products/COR-CME-Catalog.php>

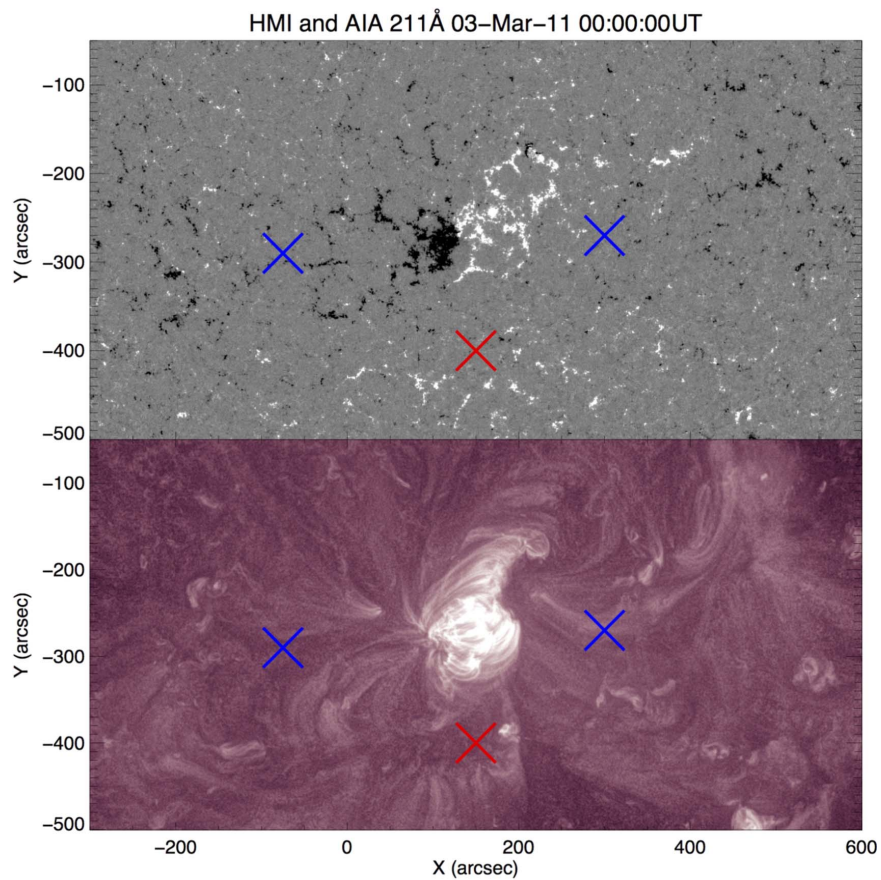


Figure 5. Top panel: HMI magnetograph. A small AR (NOAA AR 11165) is located in the center of the image, with a polarity inversion line in a north–south direction. A second polarity inversion line runs in an east–west direction, where a filament channel is present. Bottom panel: MGN-processed *SDO*/AIA 211 Å image. NOAA AR 11165 is located in the center of the image. The filament channel runs in an east–west direction, southeast of the AR. A filament lies to the west of the AR. The red cross represents the triangulated region (Pevtsov et al. 2012). The two blue crosses represent the footpoints of the structure as derived from the GCS model.

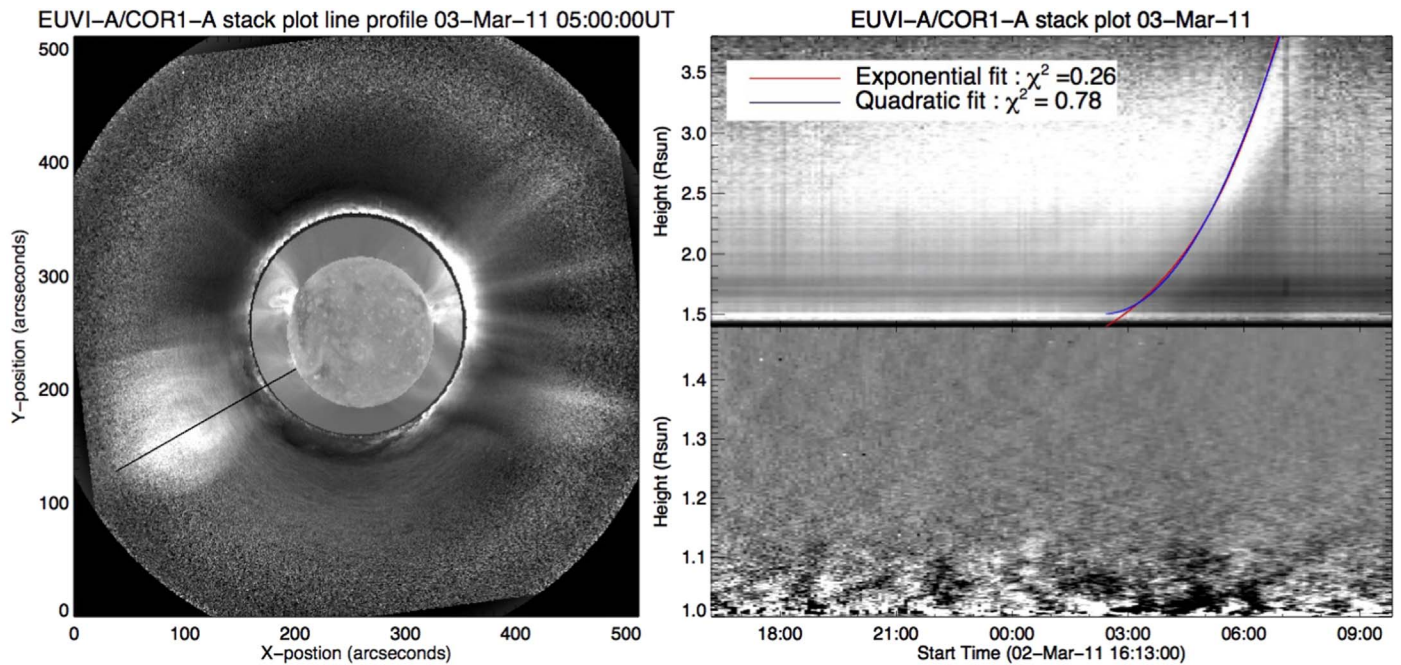


Figure 6. Left: EUVI/COR1 image indicating the slice used to create the stack plot. Right: EUVI-A 195 Å (lower) and COR1-A (upper) stack plots. The height–time profile of the stealth CME observed on 2011 March 3 can be determined from the COR1-A data, which show the cavity underside (concave-up structure) of the stealth CME. Exponential (red line) and quadratic (blue line) fits have been applied to the COR1-A data.

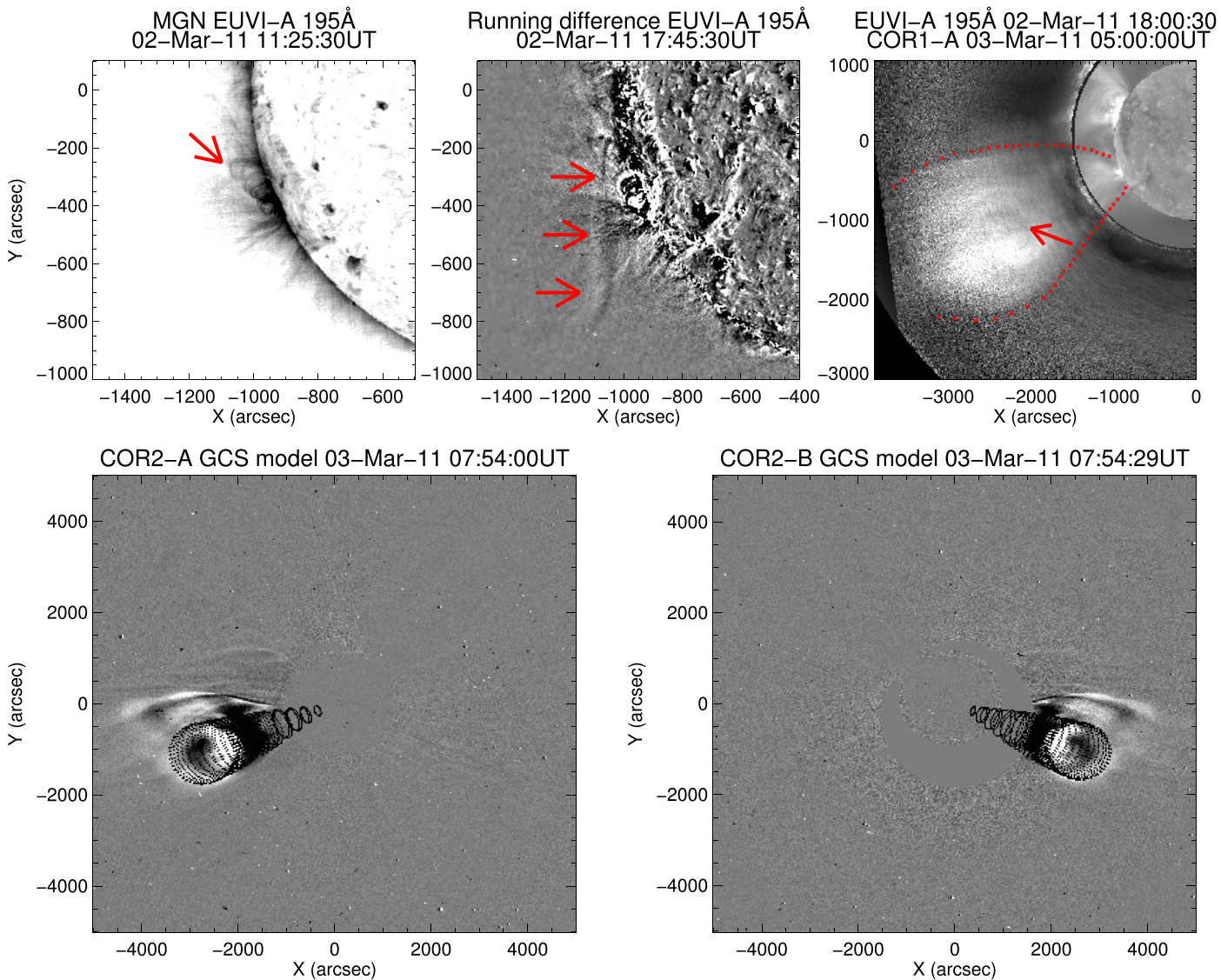


Figure 7. Top left: MGN-processed EUVI-A 195 Å image. An expansion of bright loops was observed to the north of the AR, indicated by the arrow. Top middle: time difference EUVI-A 195 Å image, with a 30-minute temporal separation. A structure was observed stretching from the north to the south and traveling outward from the solar disk, indicated by the red arrows. Top right: combined EUVI-A 195 Å and COR1-A image. The combination illustrates how the bulb structure in the EUVI images prior to the eruption expands into the CME structure observed in the COR1 images, outlined by the two dotted lines. Bottom: wire frame fitted to the CME in COR2-A (left) and COR2-B (right).

have been able to identify various dynamic structures that temporally and spatially correlate between the data sets and that together enable an investigation of the corona in the lead-up to the time of the eruption. Around 17:00 UT on 2011 March 1, a filament is observed to begin to rise and gradually erupt over approximately a 6 hr period. It is noted that the CME produced by this filament eruption is observed in the COR1-A field of view approximately 23 hr before the stealth CME. The filament eruption creates new loops that connect the eastern side of the filament channel with the west side of AR 11165. The AIA data show that from ~05:00 UT on 2011 March 2, a number of loops at the periphery of the AR 11165 begin to reconfigure. On the east side of the AR, a loop is observed to have been disconnected from an area in the northern part of the AR. It then swings up and over the AR in an anticlockwise direction at ~05:15 on UT 2011 March 2. This structure is seen in EUVI data to be almost parallel to the solar limb and in motion at ~06:10 UT on 2011 March 2. The loop expands with a north-

south motion and is shortly followed by the creation of a new, larger-scale loop system in the north of the AR. These new loops are observed in both the AIA and EUVI-A data (Figure 7, left panel). The activity observed in AR 11165 using EUV data also includes the formation of a pair of faint flare ribbons and their associated loops, which are located at the edge of the magnetic bipole away from the internal polarity inversion line. AIA 211 Å and AIA 304 Å data indicate that the flare ribbons form at ~09:00 UT on 2011 March 2, with a second phase of brightening and expansion away from the center of the AR at ~21:40 UT on 2011 March 2. This location and evolution indicate the occurrence of magnetic reconnection in a region above the AR loops. A flow of plasma is seen moving out from the south of AR 11165 from ~08:35 UT on 2011 March 2, and a second flow follows at ~13:55 UT on 2011 March 2. The visible end of the second flow appears to be immediately followed by a structure that is again almost parallel to the limb, stretching across from the north to the south, and expanding

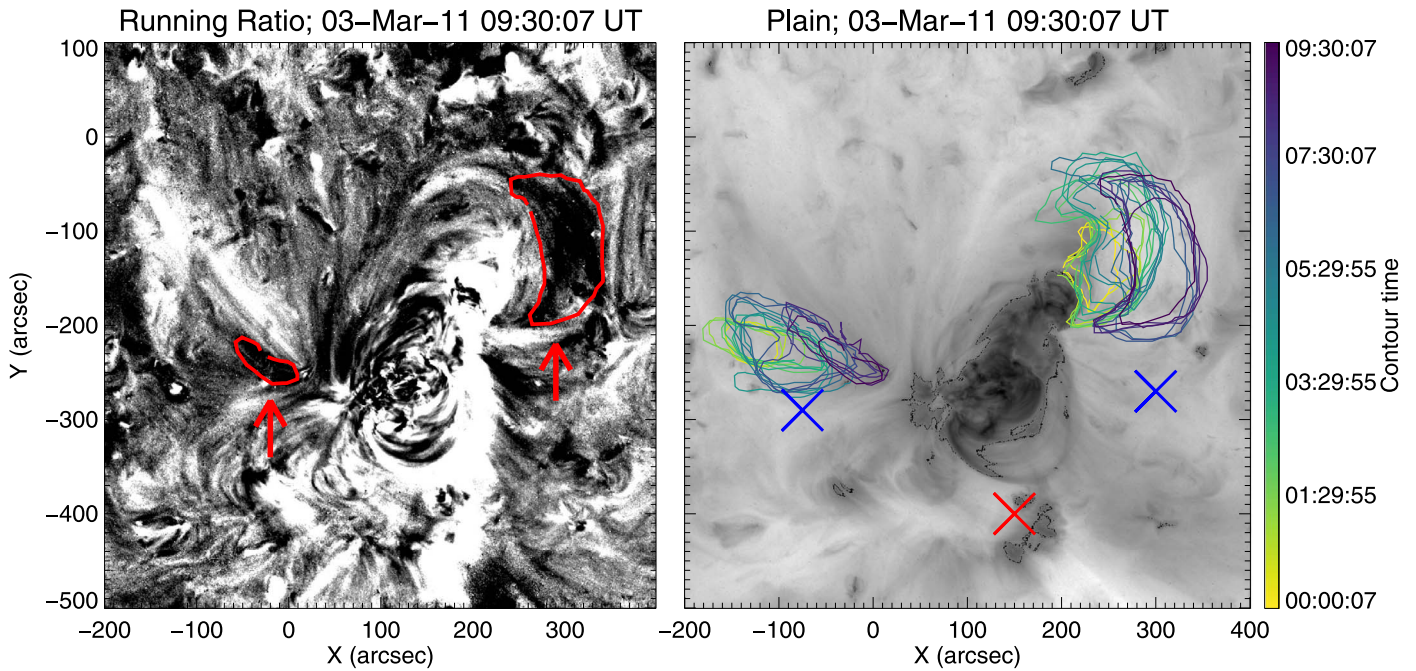


Figure 8. Left: AIA 211 Å running ratio image at the final time of EUV dimming tracking. Right: AIA 211 Å plain image, with inverted color table showing the evolution of the dimming regions north and east of the AR, outlined with contours. The dimming regions evolved over a 9 hr period. Both images are de-rotated to the start time: 00:00 UT 2011 March 3.

outward from $\sim 17:50$ UT on 2011 March 2 (Figure 7, middle panel). Fainter flows consequently move outward for a short period from $\sim 22:10$ UT on 2011 March 2. New loops slowly begin to form in the early hours of 2011 March 3, and given their close association with the CME observed in *STEREO-A* COR1 data and EUV dimmings, they are termed post-eruption loops. These post-eruption loops grow larger over a 6 hr period. Combined EUVI-A 195 Å images and COR1-A images at different times show that a bulb-shaped structure with a roughly circular center is observed to move out of the EUVI-A images into COR1-A images, where it becomes the stealth CME studied here (Figure 7, right panel). The clear circular cavity present in the center of the CME seen in the COR1-A is suggestive of a flux rope configuration at this time.

Running difference images and running ratio images with 30-minute temporal separation revealed two faint dimming regions located on either side of AR 11165 (Figure 8(a)), which both match with those found by Nitta & Mulligan (2017) and are not too far from where the footpoints estimated from the GCS model were found to be. We can therefore conclude that these two dimmings are representative of the footpoints of the erupting stealth CME. As can be seen from Figure 8(b), the dimming region to the northwest of the AR both grew in size and moved away from the AR between 00:00 UT and 09:30 UT 2011 March 3, while the dimming region to the east of the AR grew in size initially and then shrunk back down in size. There is an indication that the dimmings underwent a slight clockwise rotation between 00:00 UT on 2011 March 3 and 09:30 UT on 2011 March 3. It is notable that the eastern dimming region is located in the same area as the footpoint of the dynamical structure that pulled and twisted out at $\sim 05:15$ UT on 2011 March 2, indicating a connection between the structure involved in the dynamics prior to the CME and the erupting field.

Looking at the photospheric evolution of the region, NOAA AR 11165 began to emerge on the Sun on 2011 February 25 in the eastern hemisphere and into the magnetic field of a

previously decayed AR. AR 11165 emerged at the polarity inversion line of the decayed preexisting region and with the same field orientation (positive leading magnetic field). At the time of the stealth CME on 2011 March 3, the AR had a bipolar configuration and very dispersed magnetic field having been acted on by supergranulation. Two episodes of flux emergence occurred in AR 11165 between its first appearance on disk and the time of the stealth CME, at 22:40 UT on 2011 February 25 and 06:30 UT on 2011 February 28. The evolution of the photospheric field is dominated by flux emergence rather than flux cancellation. The polarity inversion line above which the CME originated (as determined from dimmings and post-eruption loops) was oriented in a north–south direction, indicating that differential rotation had not yet had a significant effect on the AR’s configuration (Figure 5). To the south of the AR lies a polarity inversion line that is associated with an (empty; Pevtsov et al. 2012) filament channel. This inversion line was initially thought to be the location of the origin of the stealth using triangulation (Pevtsov et al. 2012).

Lastly, we looked at the radio emission of the region. The second flow observed in EUV data at $\sim 13:55$ UT on 2011 March 2 coincides with a brightening in radio frequencies around 150 MHz. The brightening was imaged by the Nançay Radioheliograph (Kerdraon & Delouis 1997) most prominently at 150 MHz between 13:52 and 14:02 UT (Figure 9). The emission arises from a source that appears to the south of NOAA AR 11165, as viewed in the plane of the sky. This spatially and temporally corresponds to the second flow observed in EUV data. The impulsive nature of the radio emission implies that particle acceleration occurs in conjunction with this second flow of plasma that is seen around 13:55 UT. Assuming second harmonic plasma emission, as the polarization is less than 10%, the 150 MHz emission corresponds to an altitude of 0.34 solar radii (238 Mm) using the Newkirk coronal density model (Newkirk 1961). The emission is not observed above 173 MHz by the Nançay

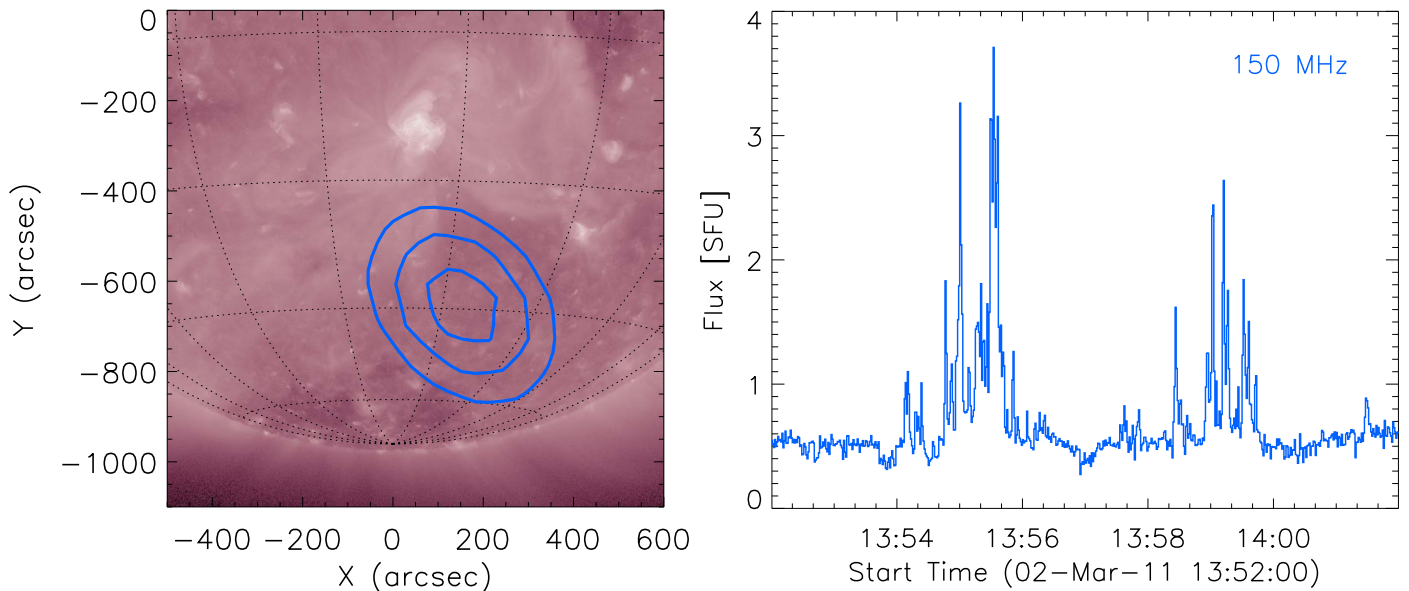


Figure 9. Left: image at 13:55 UT showing the 50%, 70%, and 90% 150 MHz radio contours superimposed on the AIA 211 Å image. Right: flux profile at 150 MHz.

Radioheliograph, restricting it to these higher coronal altitudes. This coincides with the lack of structure observed in the EUVI stack plots being a result of a high-altitude structure, supporting a hypothesis that the stealth CME was ultimately the result of a reconfiguration of high-altitude magnetic field, above the AR core, that may have involved magnetic reconnection. The faint radio emission is not visible at lower wavelengths below 150 MHz, detected by full-Sun spectrometers, so we cannot confirm whether the emission is a type III burst, caused by propagating electron beams (e.g., Reid & Ratcliffe 2014), or localized electron acceleration more in line with a type I burst (Kai et al. 1985).

Normal CMEs can have a multitude of accompanying radio emission, particularly from the upper solar corona. The stealth CMEs do not have any accompanying type II radio emission. The slow speed of stealth CMEs means that we do not expect it to drive a shock, where shock-driven acceleration can generate type II radio emission. Faster, more intense CMEs can also display moving type IV emission (James et al. 2017), generated via gyrosynchrotron emission by trapped, high-energy particles within the CME. Normal CMEs that have associated flares are frequently accompanied by type III bursts, signatures of accelerated electron beams escaping the Sun. Given the apparent high altitude of the stealth CMEs, if any electron beams are accelerated during the magnetic instability that initiates the CME liftoff, we might expect to detect faint, lower-frequency (<100 MHz) type III emission. The emission that we observe on March 3 is very faint, and brief considering the duration of the stealth CME liftoff, with no low-frequency emission observed using the full-disk integrated radio spectrometers. A future imaging spectroscopy task for the new, high sensitivity radio interferometers like the Low Frequency Array (LOFAR; van Haarlem et al. 2013) and the upcoming Square Kilometre Array (SKA).

3.2.2. Overall Remarks

The combined analysis of the activity in the lower corona as observed on disk and at the limb and the CME propagation as seen in coronagraph data together indicate that the stealth CME

of 2011 March 3 originated in AR 11165. The MGN technique enhanced subtle changes in the evolution of plasma emission structures consistent with changes in the magnetic field configuration of the AR. EUV dimmings at the periphery of the AR, the lack of opening of the AR arcade field, and the side-on view afforded by the *STEREO* spacecraft reveal that the erupting structure originated at a relatively high altitude above the core AR loops that dominated the EUV emission. The lack of significant flux cancellation in the AR also suggests that the scenario of low-altitude flux rope formation and eruption of van Ballegoijen & Martens (1989) does not occur here.

In the hours leading up to the stealth CME, AR 11165 and the surrounding corona undergo some notable activity. First is the eruption of a filament immediately adjacent to the AR on its western side. The filament eruption reconfigures the coronal field and produces new connections between the filament channel and AR 11165. Such an eruption may have altered the corona above the AR. In addition, prior to the stealth CME, activity was also in AR 11165 itself. The formation of new EUV loops from ~05:00 to ~06:00 UT on 2011 March 2, without any observed flux emergence at this time, is suggestive of coronal reconnection, which may have played a role in creating the pre-eruptive field.

4. Discussion

Both events were determined to be Earth directed using triangulation and GCS modeling. MGN image processing was applied to *SOHO*/EIT, *SDO*/AIA, and *STEREO*/EUVI data. As shown by Alzate & Morgan (2017), such an approach revealed subtle changes in the coronal emission structures that were not identifiable in the unprocessed data. For example, within the EUVI-A processed images, several structures were seen moving outward from the solar limb, the timings of which correlated to dynamic structures observed in the sharpened AIA images as seen on disk and the white-light CMEs seen in the coronagraph data. Indeed, the enhanced EUV images were able to reveal several observational phenomena that are in line with the CSHKP standard model of an eruption, including dimming regions and post-eruption arcades. Such lower coronal

Table 2
Table Summarizing the Timeline of the Activity Evolution Related to the Two Stealth CME Events

	Event 1: 27 Oct 2009	Event 2: 2011 Mar 3
Previous adjacent eruption	11:25 UT 2009 Oct 26	17:00 UT 2011 Mar 1
Flares and/or ribbons		09:00 UT 2011 Mar 2 21:40 UT 2011 Mar 2
Slow-rise phase	~23:00 UT 2009 Oct 26	
Flares and/or ribbons	~04:49 UT 2009 Oct 27 ~07:05 UT 2009 Oct 27	09:00 UT 2011 Mar 2 21:40 UT 2011 Mar 2
Fast-rise phase onset	13:00 UT 2009 Oct 27	...
Dimming onset	...	00:00 UT 2011 Mar 3
Post-eruption loop formation onset	13:00 UT 2009 Oct 27	00:00 UT 2011 Mar 3

signatures were observed in both stealth CME events and indicate that they originated in NOAA AR 11029 and AR 11165, respectively, contrary to previous work that has suggested that stealth CMEs might in some way be associated with open magnetic field regions, the quiet Sun, or empty filament channels. Our findings support previous work by Alzate & Morgan (2017), who showed that imaging processing techniques are essential in searching for the origins of CMEs that leave no obvious signatures on disk.

The identification of low coronal signatures associated with the CSHKP model enables us not only to identify the source region of stealth CMEs but also to analyze the evolution of each region in the time leading up to the eruption for comparison with CME theories. Models that have specifically been suggested as being relevant to stealth CMEs are those of streamer blowout CMEs (Howard & Harrison 2013) that invoke differential rotation as the mechanism that energizes the magnetic field system to bring it to an eruptive state (Vourlidis & Webb 2018). In this scenario, the pre-eruptive magnetic field configuration could be that of an arcade or a flux rope. In the streamer blowout numerical model of Lynch et al. (2016), the pre-eruptive magnetic field configuration is that of a sheared arcade energized via photospheric shearing motions within a multipolar field configuration. The shearing motions lead to breakout reconnection above the central arcade followed by flare reconnection within the sheared arcade, which forms a flux rope and accelerates the CME. The key role of photospheric flows in the above-mentioned model implies that extended polarity inversion lines should be present in stealth CME regions. We note that we do not see such extended size scales in either of our stealth CMEs. In light of this, we will go on to analyze further the source region characteristics and discuss them in the context of CME models in general.

Even though both stealth CMEs originated in ARs without extended polarity inversion lines, they were both formed in a magnetic field configuration that was extended in altitude, as found by Robbrecht et al. (2009), D’Huys et al. (2014), and Alzate & Morgan (2017). For example, *STEREO* data for the 2009 October 27 event showed that the underside of the erupting structure (as determined from the concave-up feature) was clearly visible at $0.5 R_{\odot}$ above the photosphere during its slow-rise phase, with the transition to the fast-rise phase occurring at $\sim 1 R_{\odot}$. These values are similar to those found in Robbrecht et al. (2009). Such a high altitude means that the erupting structure originated in a region with lower plasma density and weaker magnetic field than is usually found for AR CMEs. The eruptions did not originate in the core AR magnetic field of NOAA AR 11029 and AR 11165 that is responsible for the dominant AR EUV or soft X-ray emission. This high-

altitude location in turn leads to CMEs that have low accelerations due to the low magnetic field strength.

For both events COR1-A stack plots show the propagation of the *underside* of the stealth CMEs, not the leading edge of the erupting structure. However, it was not possible to identify the underside of each erupting structure in the EUVI-A stack plots, presumably due to weak plasma emission in the 195 \AA wave band associated with a low plasma density due to their high altitude. It is notable that when the stealth CME of 2009 October 27 is in its slow-rise phase (that is, before the reconnection associated with the fast-rise phase sets in) a flux rope is already present. The flux rope is identified through the concave-up structure seen in *STEREO* coronagraph images, and this observation is supportive of a pre-eruptive flux rope having formed. Both events show a clear cavity with a concave-up structure, indicating the presence of a flux rope, during the fast-rise phase. This is expected since, regardless of the pre-eruptive configuration, flare reconnection within a sheared arcade will always build a flux rope.

The challenge now is to try to discern whether any aspects of the evolution of NOAA AR 11029 that produced the 2009 October 27 event can be linked to the formation of the flux rope prior to its slow-rise phase. There is increasing observational support for the importance of the role of magnetic reconnection in the formation of eruptive structures. Observationally this is manifested by (confined) flaring or flux cancellation that is able to transform a sheared arcade into a flux rope. The height of the reconnection then determines the height at which the underside of the flux rope is located from the photosphere/chromosphere (Chintzoglou et al. 2015) into the corona (e.g., James et al. 2017, 2018). *SDO*/HMI and *SOHO*/MDI images of both stealth CME source regions in this study showed no major or sustained flux cancellation in the time leading up to eruption, nor were any S-shaped plasma emission structures observed in the AIA, EIT, or EUVI passbands that may have indicated the formation of a flux rope that could then have risen above the AR core. However, NOAA AR 11029 showed weak flaring in the hours leading up to the stealth CME (Table 2; top panel of Figure 10). The flaring will have been due to reconnection in the corona, and this reconnection could have produced the flux rope in the corona. Even though there is no observational support for the presence of a pre-eruptive flux rope for the stealth CME event of 2011 March 3, it is notable that flaring and flare ribbons are observed in NOAA AR 11165 in the hours leading up to the eruption. Both stealth CME source regions show a similar evolution in this regard.

Previous studies of stealth CMEs have suggested that they may be sympathetic eruptions triggered by a reconfiguration of overlying field, and therefore removal of stabilizing flux, due to

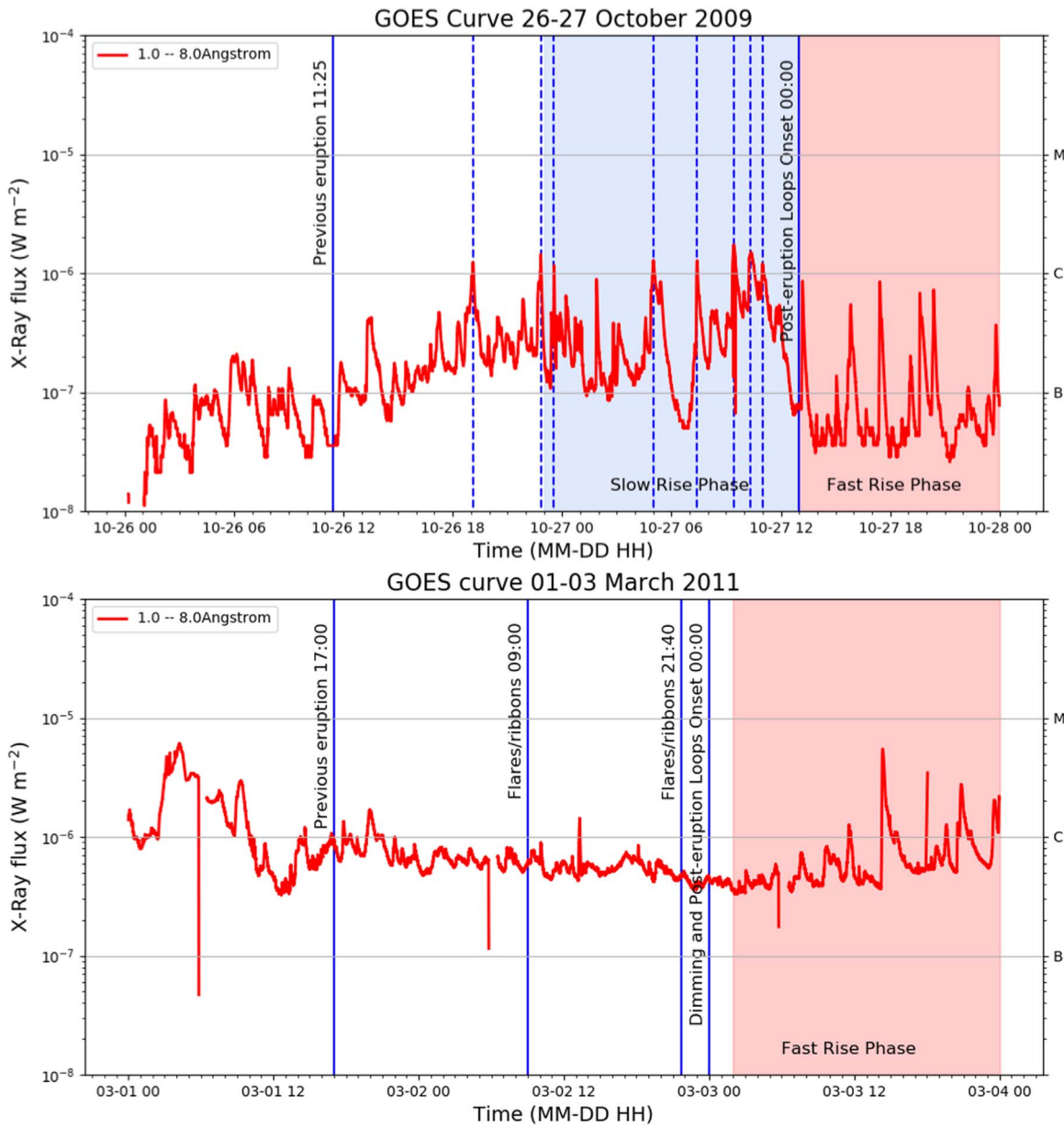


Figure 10. Top: annotated *GOES* curve for the time leading up to the stealth CME of 2009 October 27. AR 11029 was the only AR on disk at this time. The dashed lines represent C-class flares from AR 11029. The light-blue shaded region represents the time of the slow-rise phase of the stealth CME, and the light red shaded region represents the CME fast-rise phase. Bottom: annotated *GOES* curve for the time leading up to the stealth CME of 2011 March 3. There were multiple ARs in the northern hemisphere during this time, which contribute to the *GOES* light curve. The light red shaded region represents the stealth CME fast-rise phase; the slow-rise phase was not captured.

a nearby CME. Indeed, the 2009 October 27 event had an eruption from a nearby region 11.5 hr before its slow-rise phase was observed, and the event of 2011 March 3 had an adjacent eruption 31 hr before its CME-related dimming was observed (Table 2; bottom panel of Figure 10). In the absence of extended polarity inversion lines and sustained shearing motions, a sympathetic eruption suggests the presence of a preexisting flux rope in quasi-equilibrium (Török et al. 2011), which is what we find for the event of 2009 October 27.

A fundamental aspect of CMEs is that they are known to be the result of an energy storage and release process (see Green et al. 2018, for an overview). As discussed above, theoretical and modeling work on stealth CMEs has proposed that the energy injection is provided by slow shearing motions created

by photospheric differential rotation. However, in this study the stealth CMEs come from ARs with a short polarity inversion line oriented in the north–south direction and therefore are not significantly acted on by differential rotation. However, the ARs in which both events originated exhibited flux emergence, which could have been the process by which the energy was injected.

The question raised by this study is then whether stealth events represent the high-altitude part of a spectrum of CMEs, related to flux rope formation by high-altitude magnetic reconnection. Structural changes occur above the core field of both ARs, and we suggest that the stealth CMEs originate from magnetic field whose footpoints are embedded on either side of each AR. The vertical extent of each eruptive structure presents additional challenges in

terms of reconstructing the magnetic field configuration from photospheric magnetic field extrapolations and numerical modeling to capture the formation of the structure.

The availability of 195 Å data from both *SOHO*/EIT and *STEREO*/EUVI for the first stealth CME event means that it presents an interesting case study for investigating the possible role instrument capabilities play, as highlighted by Howard & Harrison (2013). Despite applying the MGN image processing techniques to *SOHO* EUV data, little could be observed in comparison to the *STEREO* EUV data. Observational limitations are clearly shown in this case, as more features could be distinguished in the *STEREO*/EUVI data. Consideration should therefore be given to temperature response, dynamic range, and image cadence during operation in the development of future EUV imagers. The key aspect is to design telescopes that are able to detect CMEs with weak signatures in EUV. This study supports the growing focus on the so-called middle corona and the need for instrumentation that can capture the evolution of structures with faint EUV emission. In the future, with more appropriate instrumentation, what would have been classed as a stealth CME in the *SOHO* or *SDO* era may no longer be the case. In addition, we find that the side-on view provided by *STEREO* was crucial in identifying, and studying the evolution of, the stealth CME source regions that were challenging to observe from above owing to the dominance of emission from the AR core. Nonetheless, understanding what causes these events to have such weak signatures but still produce magnetic structures that escape the Sun remains to be investigated further, and will aid overall understanding of the physical processes involved in CME initiation.

5. Conclusions

This study used advanced image processing techniques to identify and study the source regions of two stealth CMEs that were observed in multispacecraft coronagraph data on 2009 October 27 and 2011 March 3. We find that both stealth CMEs originated in AR areas as opposed to the quiet Sun or in filament channels, contrary to the previous studies on these stealth events (Pevtsov et al. 2012; Kilpua et al. 2014). However, the erupting structures were not formed in the core AR field, but likely at altitudes of $\sim 0.5 R_{\odot}$ above the photosphere. The energy injection appears not to be the result of differential rotation but instead to be related to the emergence of new flux into the AR. In the event of 2009 October 27 we find observational support for the presence of a flux rope formed by reconnection in the corona during or before the slow-rise phase of the CME. The flux rope may have been destabilized as a sympathetic eruption following a nearby CME. We find that the stealth CMEs of this study are no different from other CMEs in that they show features of the standard model but at the lower-energy end of the spectrum with weaker signatures that current instrumentation can only just resolve.

J.R.O. thanks the STFC for support via funding given in her PHD studentship. J.R.O. also thanks Mathew West and Marilena Mierla for useful discussions at the Royal Observatory Belgium. L.M.G. acknowledges support through a Royal Society University Research Fellowship and through the Leverhulme Trust Research Project grant 2014-051. D.M.L. acknowledges support from the European Commission’s H2020 Programme under grant agreements GREST No. 653982 and Pre-EST

No. 739500, as well as support from the Leverhulme Trust for an Early-Career Fellowship (ECF-2014-792), and is grateful to the Science Technology and Facilities Council for the award of an Ernest Rutherford Fellowship (ST/R003246/1). H.R. acknowledges support from the STFC consolidated grant (ST/P000533/1). The authors thank the anonymous referee, whose comments helped to improve the paper. *SDO* is a mission of NASA’s Living With a Star Program. *STEREO* is the third mission in NASA’s Solar Terrestrial Probes program. *SOHO* is a mission of international cooperation between ESA and NASA. The authors thank the *SDO*, *STEREO*, and *SOHO* teams for making their data publicly accessible.

ORCID iDs

Jennifer O’Kane  <https://orcid.org/0000-0002-8806-5591>
 Lucie Green  <https://orcid.org/0000-0002-0053-4876>
 David M. Long  <https://orcid.org/0000-0003-3137-0277>
 Hamish Reid  <https://orcid.org/0000-0002-6287-3494>

References

- Alzate, N., & Morgan, H. 2017, *ApJ*, **840**, 103
 Antiochos, S., DeVore, C., & Klimchuk, J. 1999, *ApJ*, **510**, 485
 Brueckner, G., Howard, R., Koomen, M., et al. 1995, *SoPh*, **162**, 357
 Burlaga, L., Sittler, E., Mariani, F., & Schwenn, A. R. 1981, *JGRA*, **86**, 6673
 Carmichael, H. 1964, *NASSP*, **50**, 451
 Cheng, X., Zhang, J., Liu, Y., & Ding, M. 2011, *ApJL*, **732**, L25
 Chintzoglou, G., Patsourakos, S., & Vourlidis, A. 2015, *ApJ*, **809**, 34
 Cremades, H., & Bothmer, V. 2004, *A&A*, **422**, 307
 Cremades, H., Bothmer, V., & Tripathi, D. 2006, *AdSpR*, **38**, 461
 Delaboudiniere, J.-P., Artzner, G., Brunaud, J., et al. 1995, *SoPh*, **162**, 291
 D’Huys, E., Seaton, D., Poedts, S., & Berghmans, D. 2014, *ApJ*, **795**, 49
 Domingo, V., Fleck, B., & Poland, A. I. 1995, *SoPh*, **162**, 1
 Druckmüller, M. 2013, *ApJS*, **207**, 25
 Green, L., Torok, T., Vrsnak, B., et al. 2018, *SSRv*, **214**, 46
 Green, L. M., & Kliem, B. 2009, *ApJL*, **700**, L83
 Green, L. M., Kliem, B., & Wallace, A. 2011, *A&A*, **526**, A2
 Hale, G. E., Ellerman, F., Nicholson, S. B., & Joy, A. H. 1919, *ApJ*, **49**, 153
 Hirayama, T. 1974, *SoPh*, **34**, 323
 Howard, R. A., Moses, J. D., Vourlidis, A., et al. 2008, *SSRv*, **136**, 67
 Howard, T. A., & Harrison, R. A. 2013, *SoPh*, **285**, 269
 James, A., Green, L., Palmerio, E., et al. 2017, *SoPh*, **292**, 71
 James, A. W., Valori, G., Green, L. M., et al. 2018, *ApJL*, **855**, L16
 Kai, K., Melrose, D. B., & Suzuki, S. 1985, *Storms* (Cambridge: Cambridge Univ. Press), 415
 Kaiser, M. L., Kucera, T., Davila, J., et al. 2008, *SSRv*, **136**, 5
 Kerdraon, A., & Delouis, J.-M. 1997, in *Coronal Physics from Radio and Space Observations*, ed. G. Trottet (Berlin: Springer), 192
 Kilpua, E., Mierla, M., Zhukov, A., et al. 2014, *SoPh*, **289**, 3773
 Kliem, B., & Török, T. 2006, *PhRvL*, **96**, 255002
 Kopp, R., & Pneuman, G. 1976, *SoPh*, **50**, 85
 Lemen, J. R., Title, A. M., Akin, D. J., et al. 2012, *SoPh*, **275**, 17
 Lynch, B. J., Masson, S., Li, Y., et al. 2016, *JGRA*, **121**, 10,677
 Ma, S., Attrill, G., Golub, L., & Lin, J. 2010, *ApJ*, **722**, 289
 Moore, R. L., Sterling, A. C., Hudson, H. S., & Lemen, J. R. 2001, *ApJ*, **552**, 833
 Morgan, H., & Druckmüller, M. 2014, *SoPh*, **289**, 2945
 Newkirk, G., Jr. 1961, *ApJ*, **133**, 983
 Nindos, A., Patsourakos, S., Vourlidis, A., & Tagikas, C. 2015, *ApJ*, **808**, 117
 Nitta, N. V., & Mulligan, T. 2017, *SoPh*, **292**, 125
 Patsourakos, S., Vourlidis, A., & Stenborg, G. 2013, *ApJ*, **764**, 125
 Pesnell, W. D., Thompson, B. J., & Chamberlin, P. 2011, *SoPh*, **275**, 3
 Pevtsov, A. A., Panasenco, O., & Martin, S. F. 2012, *SoPh*, **277**, 185
 Reid, H. A. S., & Ratcliffe, H. 2014, *RAA*, **14**, 773
 Robbrecht, E., Patsourakos, S., & Vourlidis, A. 2009, *ApJ*, **701**, 283
 Scherrer, P., Bogart, R., Bush, R., et al. 1995, in *The SOHO Mission*, ed. B. Fleck, V. Domingo, & A. Poland (Berlin: Springer), 129
 Scherrer, P. H., Schou, J., Bush, R., et al. 2012, *SoPh*, **275**, 207
 Schrijver, C. J., Elmore, C., Kliem, B., et al. 2008, *ApJ*, **674**, 586
 Stenborg, G., & Cobelli, P. 2003, *A&A*, **398**, 1185
 Stenborg, G., Vourlidis, A., & Howard, R. A. 2008, *ApJ*, **674**, 1201

- Sturrock, P. 1966, *Natur*, 211, 695
- Thernisien, A., Howard, R., & Vourlidas, A. 2006, *ApJ*, 652, 763
- Török, T., Panasenco, O., Titov, V. S., et al. 2011, *ApJL*, 739, L63
- van Ballegooijen, A. A., & Martens, P. 1989, *ApJ*, 343, 971
- van Haarlem, M. á., Wise, M., Gunst, A., et al. 2013, *A&A*, 556, A2
- Vourlidas, A., Lynch, B. J., Howard, R. A., & Li, Y. 2013, *SoPh*, 284, 179
- Vourlidas, A., & Webb, D. F. 2018, *ApJ*, 861, 103
- Vršnak, B. 2008, *AnGeo*, 26, 3089
- Wang, Y., Chen, C., Gui, B., et al. 2011, *JGRA*, 116, A04104
- Webb, D. F., & Howard, T. A. 2012, *LRSP*, 9, 3
- Zhang, J., Cheng, X., & Ding, M.-D 2012, *NatCo*, 3, 747
- Zhang, J., Dere, K., Howard, R., Kundu, M., & White, S. 2001, *ApJ*, 559, 452
- Zhang, J., & Dere, K. P. 2006, *ApJ*, 649, 1100
- Zhang, J., Richardson, I., Webb, D., et al. 2007, *JGRA*, 112, A10102